AIAA JOURNAL
Vol. 42, No. 12, December 2004

Blending Functions in Hybrid Large-Eddy/Reynolds-Averaged Navier–Stokes Simulations

X. Xiao,* J. R. Edwards,† and H. A. Hassan‡
North Carolina State University, Raleigh, North Carolina 27695-7910

Several blending functions for use in hybrid large-eddy simulation (LES)/Reynolds-averaged Navier–Stokes (RANS) simulations of shock-separated flows are tested. The blending functions shift the turbulence closure from a k–ζ turbulence model near solid surfaces to a $k-\Delta$ subgrid closure away from the wall. Three distinct forms for the blending function are developed: one that depends on the ratio of the von Kármán length scale and the Taylor microscale, another that depends on the ratio of the RANS eddy viscosity to the subgrid eddy viscosity, and a third which replaces the von Kármán length scale in the first form with the distance to the nearest wall. Comparisons are made for two cases: Mach 2.79 flow over a 20-deg compression corner and Mach 2.88 flow over a 25-deg compression/expansion corner. Inflow boundary conditions for all calculations employ the rescaling/reintroducing procedure developed by Xiao et al. (Xiao, X., Edwards, J. R., Hassan, H. A., and Baurle, R. A., "Inflow Boundary Conditions for Hybrid Large Eddy/Reynolds Averaged Navier–Stokes Simulations," *AIAA Journal*, Vol. 41, No. 8, 2003, pp. 1481–1489) for hybrid LES/RANS simulations of wall-bounded flows. In general, the blending function based on the von Kármán length scale gives the best results when compared with measured data. The skin friction predictions show the highest sensitivity to the various blending functions.

Introduction

HYBRID large-eddy simulation (LES)/Reynolds-averaged Navier–Stokes (RANS) simulations have received increased attention lately because they potentially provide a less-expensive approach than LES for studying unsteady turbulent flows where the geometry-dependent large structures play a major role in dictating the behavior of the flow. The bulk of the hybrid LES/RANS approaches make use of two distinct concepts. One advanced by Speziale[1] defines the stress tensor as

$$\tau_{ij} = [1 - \exp(-\beta\Delta/L_k)]^n \tau_{ij}^{(R)} \tag{1}$$

where L_k is Kolmogorov's length scale, Δ is a representative grid size (or filter width), $\tau_{ij}^{(R)}$ is the Reynolds stress provided by a RANS model, and β and n are model constants. Another concept is that of the detached-eddy simulation (DES) of Spalart et al.[2] In this concept, the distance to the nearest wall, d, in the Spalart–Allmaras[3] one-equation model is replaced by a new length scale:

$$\tilde{d} = \min(d, C_{\mathrm{DES}}\Delta) \tag{2}$$

where C_{DES} is a model constant. For high-Reynolds-number flows, the typical behavior of each approach is to model wall-bounded regions through RANS concepts, because the grid resolution is generally insufficient in the directions transverse to the wall normal to resolve details of near-wall eddy motion.

One potential disadvantage of the aforementioned approaches is that the transition between LES and RANS regions may depend entirely on the grid spacing and is not generally correlated with the boundary-layer development. Depending on the choice of grid scale, the RANS/LES transition can occur deep within the boundary layer or well outside. Most calculations with the DES method, in particular, are gridded such that wall boundary layers are entirely contained within the RANS region; thus, the technique is most appropriate for flows that exhibit a clear delineation between attached boundary layers at surfaces (treated as RANS) and free-shear layers or regions of massive flow separation (treated as LES).

The emphasis in our work is toward internal flows characteristic of high-speed propulsion devices. Such flows are typically dominated by shock–boundary-layer interactions, which induce local regions of embedded separated flow that may be unsteady in the mean. Even in simple shock–boundary-layer interactions, such as compression-ramp flows, RANS approaches tend to underpredict the observed rapid recovery of the boundary layer downstream of reattachment and do not account for low-frequency oscillations of the separation regions and the associated shock systems. Recent efforts[4–6] have resulted in the development of a class of zonal hybrid LES/RANS approaches for such flows, in which the clear aforementioned delineation may or may not be apparent. The term *zonal* refers to the use of flow-dependent blending functions to shift the closure from RANS in the near-wall regions to LES in the outer part of the boundary layer and in regions of local separation. The blending function may depend on local flow properties, wall distances, and a grid scale but is not restricted to depend exclusively on the grid scale. The viewpoint taken in this work is that the RANS component functions as a sophisticated form of a near-wall closure in an otherwise LES description of the flow: thus, a strong coupling of the model response with the boundary-layer structure is required.

In Refs. 4 and 6, blending functions similar in construction to those used in Menter's k–ω/k–ϵ model[7] were used to facilitate the RANS-to-LES transition. Results were obtained for Mach 2.79 flow over a 20-deg compression corner,[8] Mach 2.92 flow over a ramped cavity,[9] and Mach 2.45 flow past a blunt annular sting,[10] using Menter's model as the RANS component of the closure. A parallel investigation[5] utilized a blending function that depended on the grid scale but not on the wall distance. Results were obtained for Mach 2.88 flow over a 25-deg compression/expansion corner[11] using the k–ζ (enstrophy) model[12] as the RANS component of the closure. Reference 5 also introduced a procedure for superimposing a realistic fluctuation field onto a mean inflow profile computed from a RANS model. This approach, a variant of the rescaling/reintroducing methods used by Urbin and Knight[13] in their LES simulations, allowed for the sustenance of turbulent structures in the outer portion of the boundary layer and was found to

Received 23 April 2003; presented as Paper 2003-3462 at the AIAA 33rd Fluid Dynamics Conference, Orlando, FL, 23–26 June 2003; revision received 30 April 2004; accepted for publication 20 July 2004.

*Postdoctoral Research Associate, Department of Mechanical and Aerospace Engineering. Member AIAA.
†Associate Professor, Department of Mechanical and Aerospace Engineering. Senior Member AIAA.
‡Professor, Department of Mechanical and Aerospace Engineering. Associate Fellow AIAA.

be a critical component in predicting the upstream extent of axial separation regions.

Though encouraging results were obtained in these studies, the question of how best to design a LES/RANS blending function remains open. The present work focuses on assessing the performance of different blending functions as used with a common RANS closure (the k–ζ model) and a common subgrid closure. Three different approaches are compared in this work. One approach is independent of the distance to the nearest wall and the grid scale. Another is dependent on the distance to the nearest wall but not on the grid scale, and a third is dependent on the grid scale but not on the wall distance. Two of the approaches reach well-defined limits within the logarithmic layer and, thus, the RANS-to-LES transition may be correlated with the extent of the logarithmic region. The next section of the paper provides details of the approach, including the turbulence closure, the blending function definitions, initial and boundary conditions, and numerical method. Results are then presented for Mach 2.79 flow over a 20-deg compression corner[8] (considered previously in Ref. 6) and for Mach 2.88 flow over a 25-deg compression/expansion corner[11] (considered previously in Ref. 5).

Technical Approach

Turbulence Closure

The hybrid schemes considered in this work modify only the turbulence kinetic energy (k) equation and the eddy viscosity definition. For the k–ζ model, the k equation for the hybrid LES/RANS scheme can be written as[5]

$$\frac{\partial \bar{\rho} k}{\partial t} + \frac{\partial \bar{\rho} \tilde{u}_j k}{\partial x_j} = \frac{\partial}{\partial x_j}\left[\left(\frac{\mu}{3} + \frac{\mu_t}{\sigma_k}\right)\frac{\partial k}{\partial x_j}\right] + \tau_{ij}\frac{\partial \tilde{u}_i}{\partial x_j} - (1-\Gamma)\left(\frac{1}{C_k}\frac{\mu_t}{\bar{\rho}^2}\frac{\partial \bar{\rho}}{\partial x_i}\frac{\partial \bar{P}}{\partial x_i} + C_1\frac{\bar{\rho} k}{\tau_\rho} + \mu\zeta\right) - \Gamma C_d \bar{\rho}\frac{k^{\frac{3}{2}}}{\Delta} \quad (3)$$

where

$$\mu_t = \rho[(1-\Gamma)\nu_{t,R} + \Gamma\nu_{t,L}] \quad (4)$$

$$\nu_{t,R} = C_\mu(k^2/\nu\zeta), \qquad \nu_{t,L} = C_s\sqrt{k}\Delta$$

$$C_\mu = 0.09, \qquad C_s = 0.01 \quad (5)$$

The form for the ζ (enstrophy) equation and the undefined constants and functions in Eq. (3) may be found in Ref. 12. As the blending function Γ approaches 0.0, the closure approaches its RANS description, whereas as Γ approaches 1.0, the closure shifts to a one-equation subgrid model.

When production balances dissipation in the LES region, Eq. (3) yields a Smagorinsky-type subgrid eddy viscosity:

$$\nu_t = C_s\sqrt{C_s/C_d}|S|\Delta^2 \quad (6)$$

Both C_s and C_d are chosen as 0.01, and the filter width Δ is given as the cube root of the local cell volume.

Blending Functions

Three different hybrid blending functions are considered in conjunction with the k–ζ RANS model. All three functions shift the closure from a RANS model next to the wall to a one-equation subgrid model away from the wall. The first to be considered is explicitly independent of the grid and the geometry and is written as

$$\Gamma_{\text{vk}} = \tanh(l_{\text{vk}}/\alpha_1\lambda)^2 \quad (7)$$

where

$$l_{\text{vk}} = \frac{S}{|\nabla S|}, \qquad \lambda = \sqrt{\frac{k}{\zeta}}$$

$$S = \sqrt{S_{ij}S_{ij}}, \qquad S_{ij} = \frac{1}{2}\left(\frac{\partial u_i}{\partial x_j} + \frac{\partial u_j}{\partial x_i}\right) \quad (8)$$

and α_1 is a model constant. The length scale l_{vk} is referred to as the von Kármán length scale and is equal to the distance normal to the wall in the log-law region. The other length scale, λ, is proportional to the Taylor microscale, which is the characteristic eddy size in the inertial subrange. The inertial subrange is the region that lies between the energy-containing range representative of the large scales and the viscous range representative of the fine scales.

The second blending function is a variation on the expression given in Eq. (7) where l_{vk} is replaced by d, the distance to the nearest wall. Thus,

$$\Gamma_d = \tanh(d/\alpha_1\lambda)^2 \quad (9)$$

Note that l_{vk} is quite different from d outside the log layer.

The third blending function is the grid-scale-dependent function used in Ref. 5. Thus,

$$\Gamma_\Delta = \tanh(l_\epsilon/\alpha_2\Delta)^2 \quad (10)$$

where

$$l_\epsilon = k^{\frac{3}{2}}\Big/\nu\zeta \quad (11)$$

is the integral scale, ν is the kinematic viscosity, and $\alpha_2 = 5$ is a model constant. Using Eq. (5), it can be seen that

$$l_\epsilon/\Delta \sim \nu_{t,R}/\nu_{t,L} \quad (12)$$

It was found in Ref. 5 that Γ must be a nondecreasing function as the distance to the nearest wall increases. This requirement was implemented for Γ_{vk} and Γ_Δ by choosing

$$\Gamma_j = \max(\Gamma_j, \Gamma_{j-1}) \quad (13)$$

where j is the index of the grid cell in the normal direction. For complex shapes, it may be necessary to keep track of the distance from the nearest wall. This requirement introduces a degree of geometry dependence into the formulation. For the other blending function, where d appears explicitly, the resulting Γ is nondecreasing.

The model constants α_1 and α_2 were chosen so that Γ achieves a value of 0.5 somewhere in the log-law region. Substitution of the log region forms $k = u_\tau^2/\sqrt{C_\mu}$ and $\nu\zeta = u_\tau^3/\kappa y$ into Eqs. (7) or (9) shows that the $\Gamma = 0.5$ position occurs at $d^+ = 0.55\kappa\alpha_1^2/\sqrt{C_\mu}$, with $d^+ = u_\tau d/\nu$. For the given values $\kappa = 0.4$, $C_\mu = 0.09$, and $\alpha_1 = 25$, this places the transition at $d^+ \approx 470$, which is toward the middle of the log region for the two cases presented later. Within the log region, the argument of the hyperbolic tangent function in Eq. (10) reduces to $(d/\Delta)^2 = 0.55\alpha_2^2 C_\mu^{3/4}/\kappa$ for $\Gamma_\Delta = 0.5$. The precise location of the transition thus depends on the variation of the filter width in the direction normal to the surface.

Initialization Procedure and Boundary Conditions

Two shock–boundary-layer interactions are simulated in this work. The initialization procedure starts by obtaining a RANS solution for the flat-plate flow leading up to the interaction region. This is performed such that experimental boundary-layer properties are matched at a target location upstream of the actual interaction (given in the experimental databases and listed later). The computational inflow plane for the calculation of the interaction region is extracted from the flat-plate solution at a location 10–12 boundary-layer thicknesses upstream of the target location. A RANS solution is then obtained for the entire interaction region (see Figs. 1 and 2), and a hybrid LES/RANS solution is obtained for the flat-plate region upstream of the wedge apex. This solution provides some large-scale structural content in the incoming boundary layer and is facilitated through the use of the rescaling/reintroducing procedure described in Ref. 5. In this, the fluctuating properties are extracted from a location upstream of the wedge apex (the recycle plane), rescaled according to inner- or outer-layer scaling laws, and superimposed on the RANS mean flow at the actual inflow plane. This step does not have to be performed until a statistically stationary state is reached, because the flat-plate solution will be evolved further as part of the hybrid LES/RANS calculation of the entire domain. Figure 3 shows the initial condition for the 20-deg ramp calculation, in which the partially evolved hybrid LES/RANS solution replaces the incoming

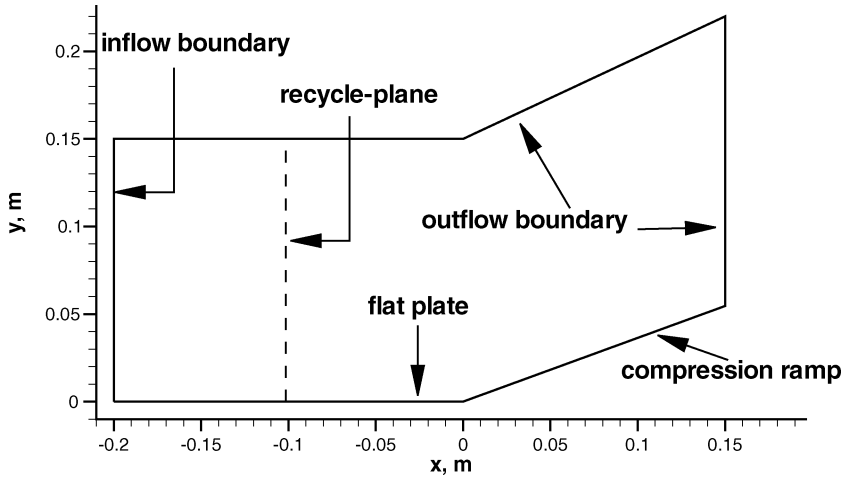

Fig. 1 Schematic of 20-deg compression ramp.[8]

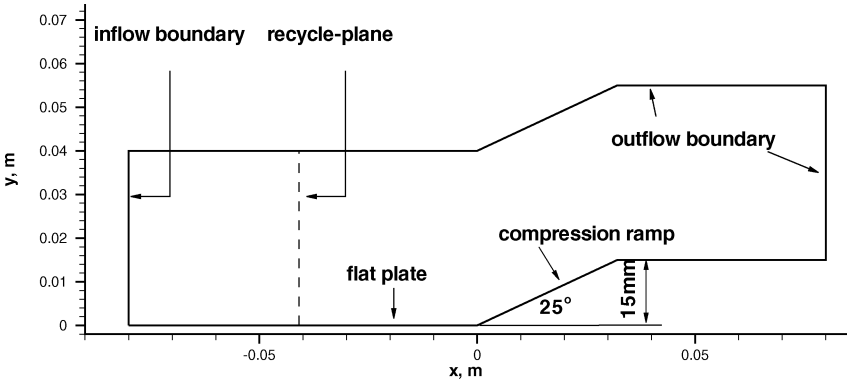

Fig. 2 Schematic of 25-deg compression/expansion ramp.[11]

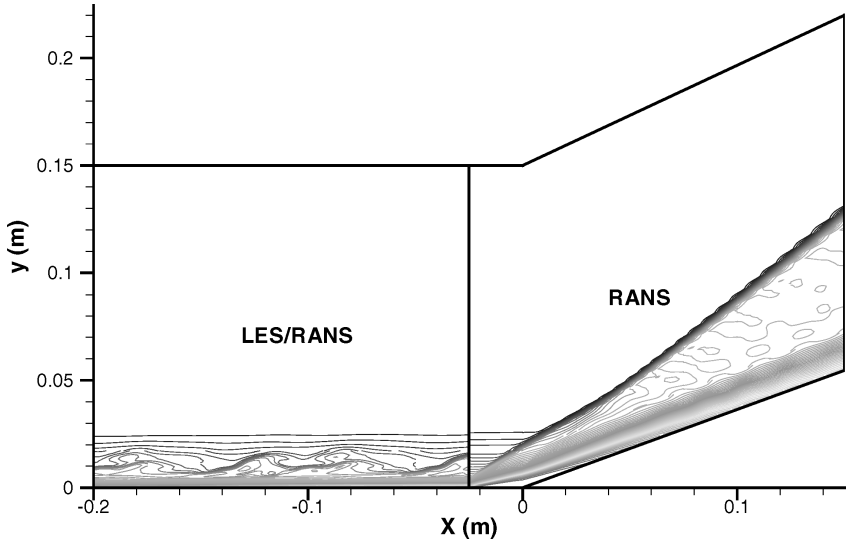

Fig. 3 Initial condition for 20-deg compression-ramp calculation: temperature contours at *X–Y* centerplane.

RANS flat-plate boundary layer. The need for this rather complicated initial condition arises from the fact that the blending functions, when applied, act immediately to reduce the eddy viscosity, making the flow much less resistant to the adverse pressure gradient. In the absence of the resolved turbulence energy from the LES component, as developed and sustained by the recycling procedures, unrestricted growth of the separation region may contaminate the recycle plane and the inflow boundary condition.

Adiabatic, no-slip boundary conditions are employed at solid surfaces and extrapolation conditions are used at the outflow boundaries. Periodic boundary conditions are employed in the spanwise (z) direction. As mentioned earlier, the recycling/reintroducing procedure of Ref. 5 is used to provide inflow boundary conditions for all cases considered.

Numerical Procedure

A second-order essentially nonoscillatory upwinding method based on the low-diffusion flux-splitting scheme of Edwards[14] is used to discretize the inviscid fluxes while central differences are employed for the viscous and diffusion terms. A planar relaxation

subiteration procedure, which results in second-order temporal accuracy, is used to integrate the system. The code is parallelized using domain decomposition and message passing interface strategies and is optimized for the IBM SP-3 architecture at the North Carolina Supercomputing Center.

Results and Discussion

Twenty-Degree Compression Ramp

A schematic of the experimental setup[8] is shown in Fig. 1, which depicts a 20-cm flat plate connected to a 20-deg ramp. The target inflow conditions are given at $x = -3.81$ cm and are summarized in Table 1. The recycle plane is located at $x = -10.3$ cm, and the actual inflow plane is located at $x = -20$ cm. The grid consists of $449 \times 129 \times 69$ nodes in the streamwise, normal, and spanwise directions. The spanwise extent is set as 2.9δ, where δ is the boundary-layer thickness at the target inflow conditions. Equal mesh spacing is used in the x and z directions, whereas the mesh spacing in the y direction is refined near the wall with $y^+ < 1$ at the first cell center off the wall. The computational domain is decomposed into 84 blocks for mapping onto the IBM SP-3 architecture. The time step employed is 1.2×10^{-7} s. The flow reaches a statistically steady condition after about seven characteristic times. One characteristic time is defined as the time necessary for a fluid particle traveling at the freestream velocity to pass through the domain and is equal to 6.23×10^{-4} s for this simulation. The simulation was continued for an additional 4.6 characteristic times to collect statistics. Instantaneous flow properties were averaged over the spanwise extent of the domain and time averaged over the 4.6 characteristic times to produce nominally two-dimensional mean-flow predictions.

A typical instantaneous velocity contour at the midpoint of the z extent is shown in Fig. 4. The further evolution of the large-scale structures in the incoming boundary layer is clearly indicated by comparing this result with the initial condition shown in Fig. 3. The local deformation of the separation and reattachment shocks due to large-eddy interaction is also indicated, as is the general decrease in the size of the organized structures in the recovery region downstream of the wedge apex. Figures 5–7 compare the wall pressure, skin friction, and velocity profiles for the hybrid LES/RANS simulations using blendings Γ_{vk} and Γ_d with two-dimensional results using the k–ζ RANS model and with experimental data. Figure 5 shows that the two blending functions yield nearly identical results for wall pressure. Both yield a lower pressure in the separated region, indicating that the initial displacement effect of the separation bubble is not as pronounced as indicated in the experiment and as predicted by the RANS model. One must recognize, however, that interactions of this type exhibit low-frequency oscillations of the separation region (which are captured by the present calculations and similar computations[6]). The period of these oscillations[15] is long enough so that the relatively short-duration sampling of the hybrid LES/RANS data may not capture a complete cycle of this motion. The RANS k–ζ model also provides better agreement with experimental skin friction data except in the vicinity of the separation region itself, where the hybrid LES/RANS models

Table 1 Twenty-degree ramp target inflow conditions at $x = -3.81$ cm

Parameter	Value
M_∞	2.79
P_∞, Pa	26001
T_∞, K	100.8
ρ_∞, kg/m^3	0.77
δ, cm	2.7

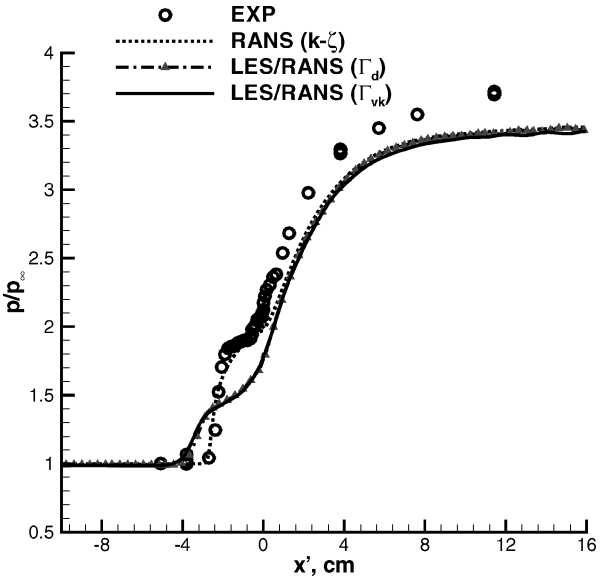

Fig. 5 Wall pressure distribution, Γ_d vs Γ_{vk} (20-deg compression ramp[8]).

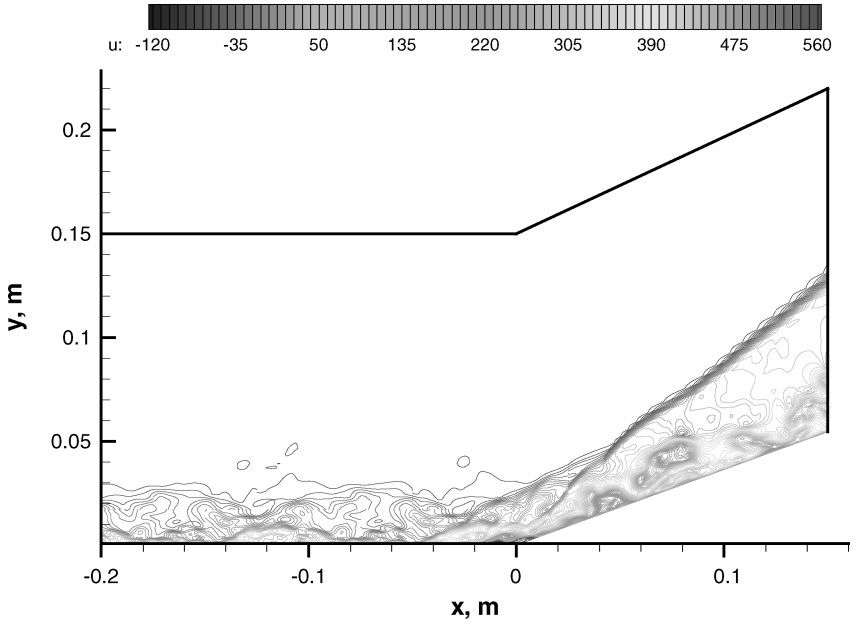

Fig. 4 Instantaneous streamwise velocity (u) contours (20-deg compression ramp[8]).

predict a lower backflow velocity (less negative skin friction coefficient). The Γ_{vk} blending results in lower overall skin friction values than the Γ_d blending. This leads to better predictions downstream of reattachment but worse agreement upstream of the separation region. Figure 7 shows that the hybrid models perform better in predicting the velocity profiles. Of particular note is the ability of both hybrid models to capture the rapid recovery of the inner part of the boundary layer downstream of reattachment, whereas the RANS model predicts both a delayed reattachment and a less-rapid recovery.

Figures 8–10 compare results of hybrid LES/RANS simulations using blendings Γ_{vk} and Γ_Δ with results from the k–ζ model and with experimental data. As may be seen from Figs. 8 and 9, the Γ_{vk} predictions are in better agreement with experiment than those of the Γ_Δ blending. Although the reattachment position is closely matched, the Γ_Δ blending results in a slight overprediction of the upstream extent of the axial separation region and provides significantly higher skin friction levels in the recovery region. Figure 10 shows that velocity-profile predictions for the Γ_Δ blending are in close accord with those of the Γ_{vk} blending except for the first two stations ($x = -3.81$ and -1.11 cm).

An indication of the relative effects of the different blending functions is shown in Fig. 11: a plot of the average kinematic eddy viscosity ν_t vs d^+ at the recycle plane location upstream of the separation zone. To give an indication of the predicted extent of the logarithmic layer, the velocity profile as predicted by the k–ζ model is also shown in wall coordinates. The effect of the blending functions in reducing the eddy viscosity (relative to that of the k–ζ RANS model) is clearly indicated. The average position of the blending functions may be indicated by the abrupt drop in the eddy viscosity value relative to its peak value. All approaches follow the RANS distribution closely in the inner part of the log region, with the Γ_{vk} prediction providing the best agreement. The $\Gamma = 0.5$ position can be correlated with the midpoint of the decaying portion of the eddy viscosity distribution. For the Γ_d blending function, this position is close to the theoretical estimate of $d^+ = 470$ but, for the others, the $\Gamma = 0.5$ position is shifted inward toward the wall. Comparing these trends with the skin friction distributions of Figs. 6 and 9, one

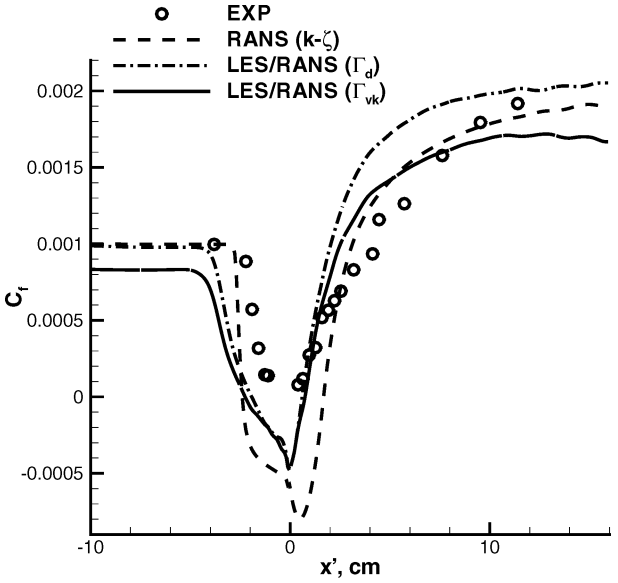

Fig. 6 Skin friction distribution, Γ_d vs Γ_{vk} (20-deg compression ramp[8]).

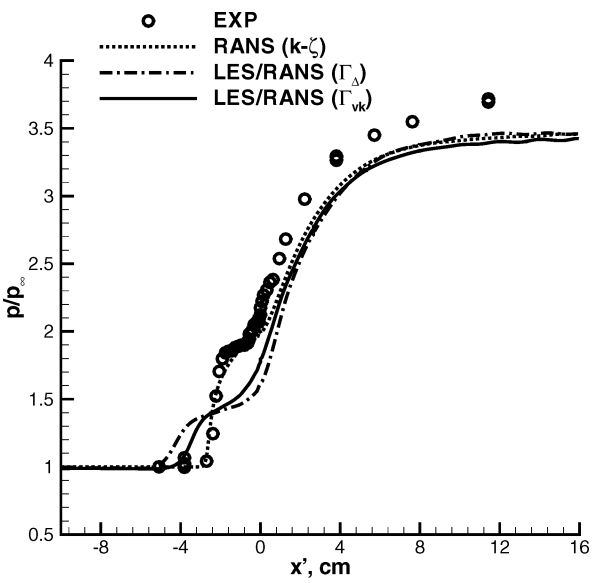

Fig. 8 Wall pressure distribution, Γ_Δ vs Γ_{vk} (20-deg compression ramp[8]).

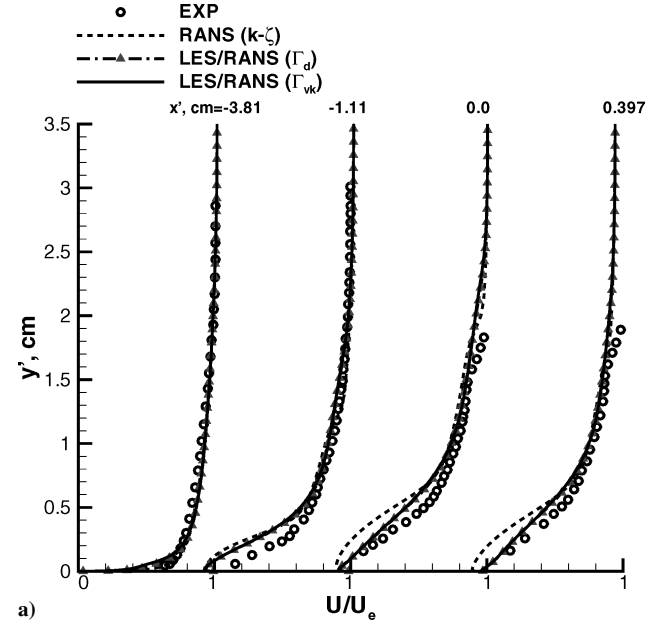

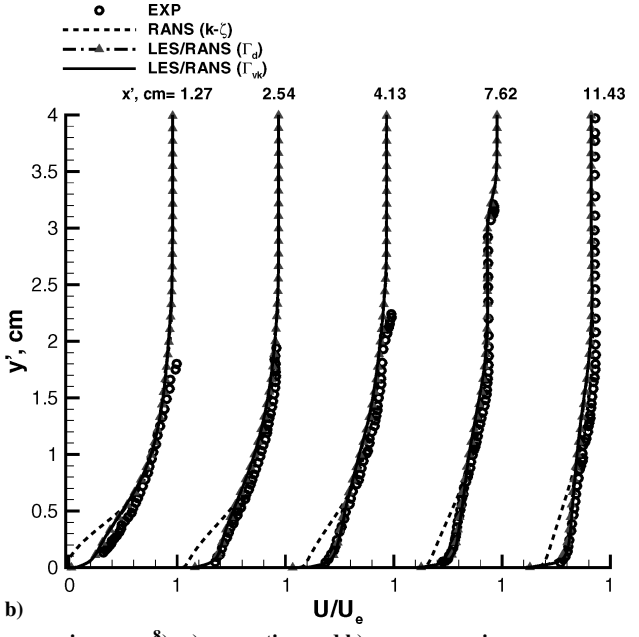

Fig. 7 Comparison of velocity profiles, Γ_d vs Γ_{vk} (20-deg compression ramp[8]): a) separation and b) recovery region.

can observe that better predictions of skin friction upstream of the interaction zone result when the RANS region extends further into the middle and outer portions of the logarithmic region.

Twenty-Five-Degree Compression/Expansion Ramp

A schematic of the 25-deg compression/expansion ramp geometry,[11] together with the relevant dimensions, is shown in Fig. 2. The target inflow conditions at $x = -3.3$ cm are presented in Table 2. The recycle plane is located at $x = -4.2$ cm, and the actual inflow plane is located at $x = -8$ cm. The grid contains $481 \times 145 \times 65$ nodes in the flow, normal, and spanwise directions, decomposed

Table 2 Twenty-five-degree ramp target inflow conditions at $x = -3.3$ cm

Parameter	Value
M_∞	2.88
P_∞, Pa	11956
T_∞, K	114.8
ρ_∞, kg/m^3	0.36
θ, mm	0.3
δ, mm	4.1

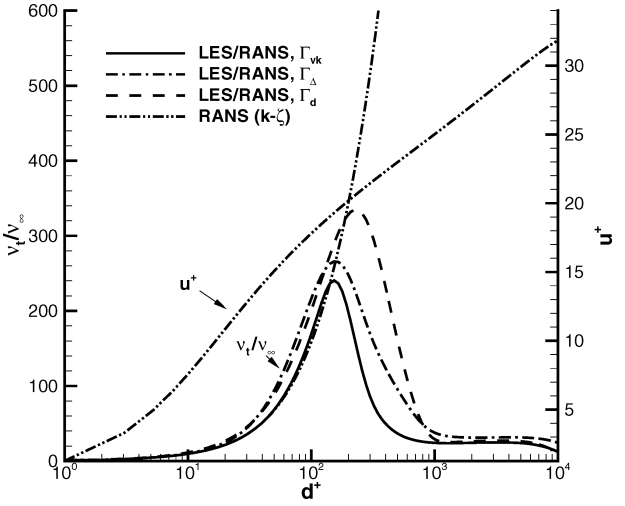

Fig. 11 Kinematic eddy viscosity vs d^+: effect of blending function (20-deg compression ramp[8]).

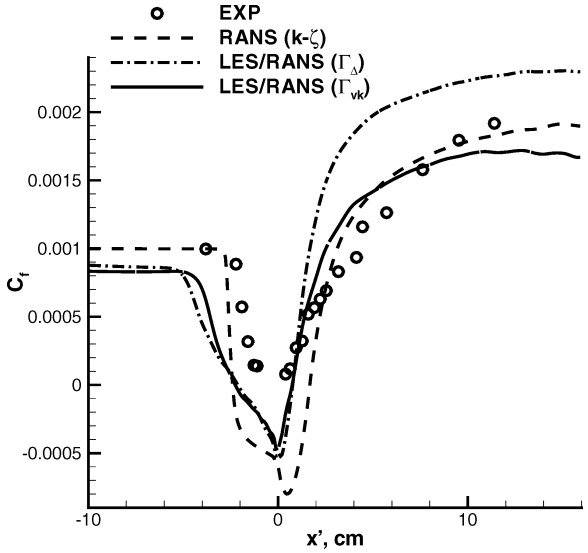

Fig. 9 Skin friction distribution, Γ_Δ vs Γ_{vk} (20-deg compression ramp[8]).

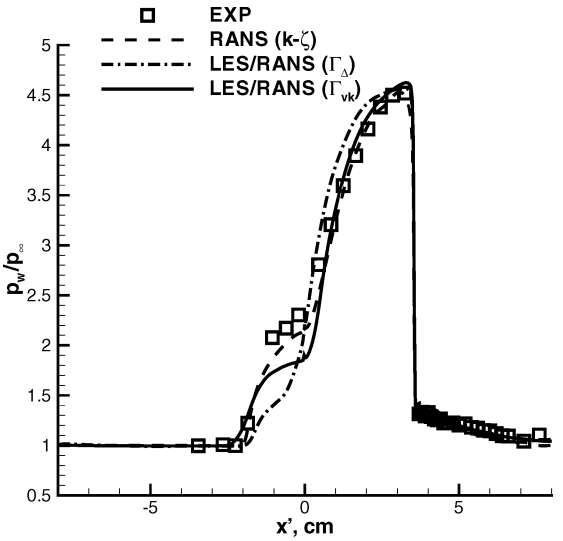

Fig. 12 Wall pressure distribution, Γ_Δ vs Γ_{vk} (25-deg compression/expansion ramp[11]).

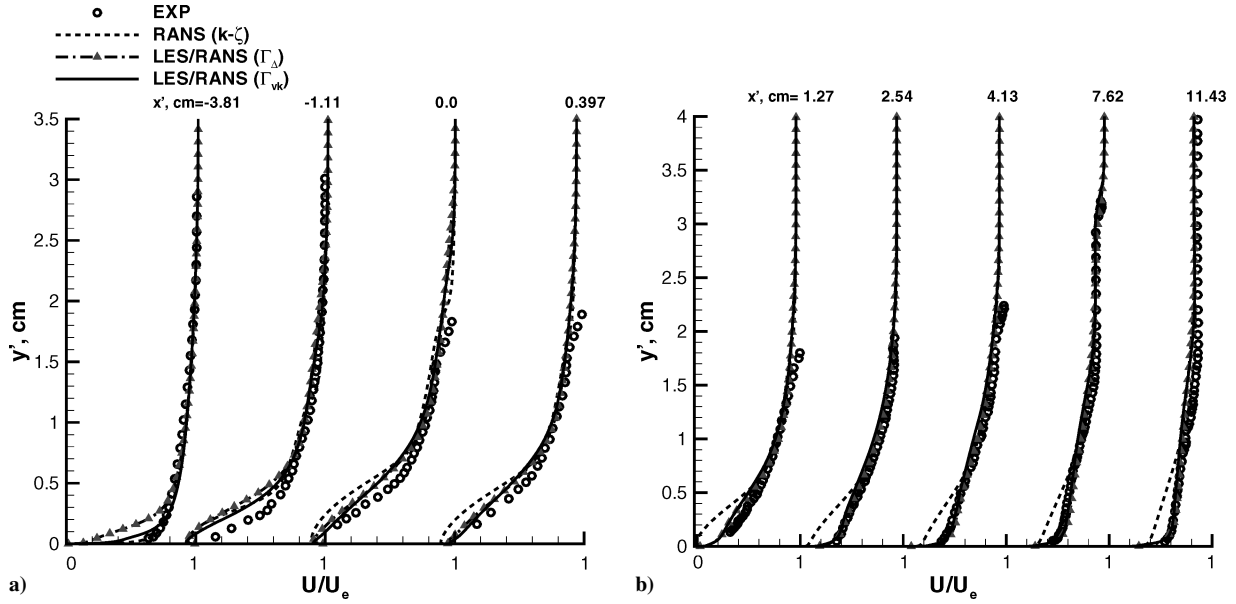

Fig. 10 Comparison of velocity profiles, Γ_Δ vs Γ_{vk} (20-deg compression ramp[8]): a) separation and b) recovery region.

into 84 load-balanced blocks. The spanwise extent of the computational domain in the z direction is 2.9 δ. This case was considered previously in Ref. 5. In that reference, grid-refinement studies were performed, and the effects of varying the model constant α_2 on the predictions provided by the Γ_Δ model were examined. Here, we compare results obtained on the finest grid with $\alpha_2 = 5$ with those obtained using the Γ_{vk} blending.

The time step employed is 6×10^{-8} s. The flow reaches a statistically steady condition after 9.2 characteristic times. One characteristic time is defined as just described and is equal to 2.59×10^{-4} s for this simulation. Additional runs over about five characteristic times were carried out to collect statistics. Boundary and initial conditions were handled in a manner identical to that of the 20-deg compression ramp.

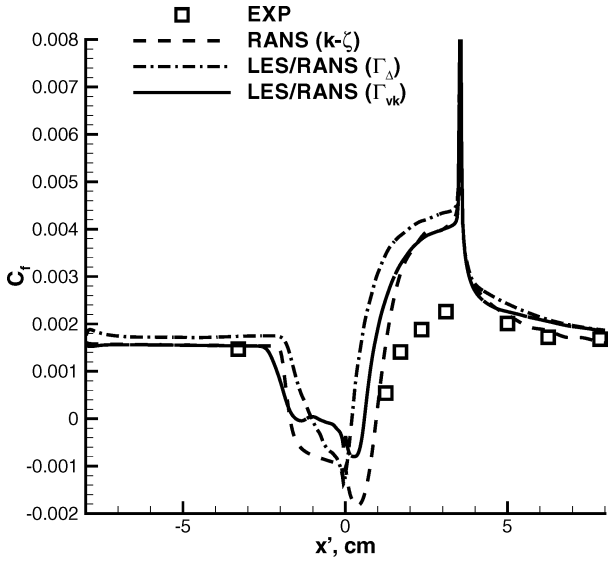

Fig. 13 Skin friction distribution, Γ_Δ vs Γ_{vk} (25-deg compression/expansion ramp[11]).

Because Γ_{vk} and Γ_d blendings gave similar results for the 20-deg ramp, only comparisons involving Γ_{vk} and Γ_Δ are shown in Figs. 12–14. Figure 12 shows that, as in the 20-deg ramp calculation, both hybrid schemes provide a lower time-averaged pressure in the separated region. Figures 12 and 13 show that both hybrid models and the k–ζ RANS model predict the upstream extent of axial separation well. In general, the Γ_{vk} blending yields pressure and skin friction distributions that are in better agreement with experiment than the Γ_Δ blending. However, neither approach gives as good agreement with experiment for these quantities as the RANS k–ζ model.

Similar conclusions hold when considering velocity profiles in the separated region, as shown in Fig. 14a. In this figure, $y' = y - y_{wall}$ and x' is measured from the compression corner. The experimental data do not indicate negative axial velocities but the "cusp" in the profile may indicate the edge of the backflow region. The Γ_{vk} blending gives better agreement with experiment than the Γ_Δ blending, but the k–ζ model gives better predictions than both hybrid models. This trend is reversed in the recovery region (Fig. 14b), where both hybrid schemes provide excellent agreement with experiment whereas the RANS model again underpredicts the rate of recovery of the velocity field near the wall.

Conclusions

This paper has compared three LES/RANS blending-function formulations with experimental data and with RANS solutions for a 20-deg compression ramp and a 25-deg compression/expansion ramp. In general, the blending function based on the ratio of the von Kármán length scale with a modeled form of the Taylor microscale (Γ_{vk}) performs the best in predicting the upstream extent of axial separation and details of the velocity field in the separation and recovery regions. This model produces a minimal amount of eddy

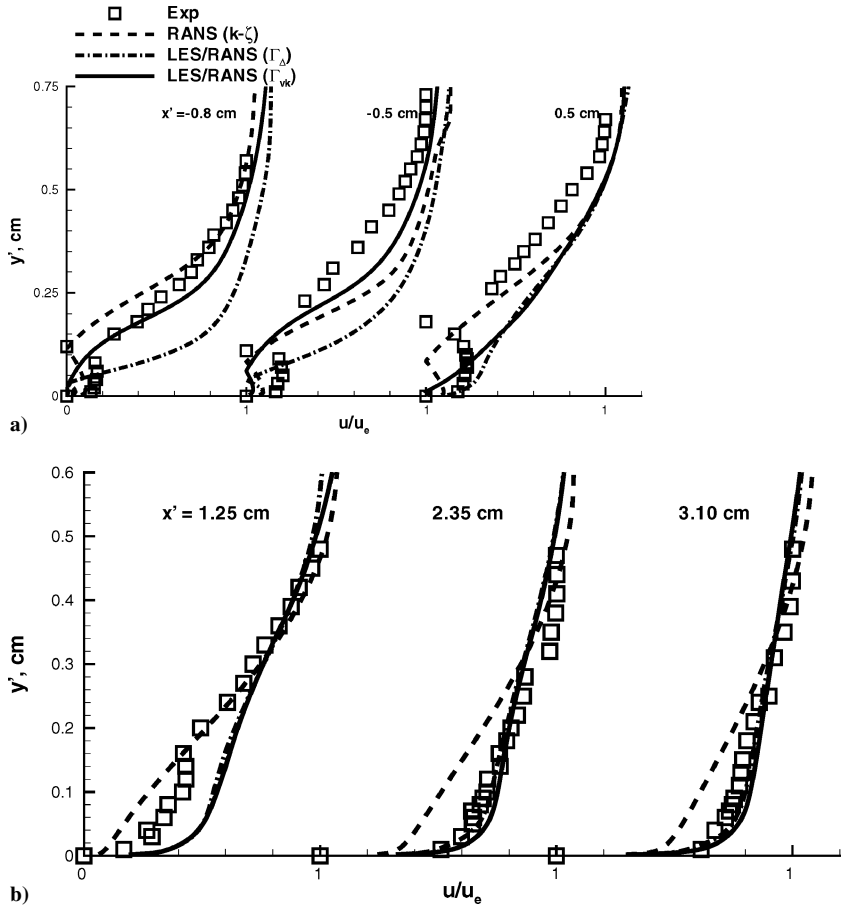

Fig. 14 Comparison of velocity profiles, Γ_Δ vs Γ_{vk} (25-deg compression/expansion ramp[11]): a) separation and b) recovery region.

viscosity, which is localized in the inner part of the logarithmic layer. The blending function based on the ratio of the wall distance with the Taylor microscale (Γ_d) produces the most eddy viscosity of the hybrid models and provides the best agreement with measured skin friction distributions upstream of the interaction zone. The blending function based on the ratio of a modeled integral scale with a filter width (Γ_Δ) provides results that are slightly inferior to the other two approaches. The RANS-to-LES transition location for the blending functions based on the Taylor microscale can be correlated as a function of the wall coordinate d^+ (at least for equilibrium turbulent boundary layers), and the actual position of the transition can be controlled by varying a model constant. This fact, plus the observed better quality of the predictions, means that Γ_{vk} and Γ_d appear more suited for future development and evaluation. Although the k–ζ RANS model compares better with experiment in predicting wall pressure, skin friction coefficient, and velocity in the separated region for the 25-deg compression/expansion ramp, it did not do as well for the 20-deg compression ramp. In both cases, the RANS model did not predict the observed rapid recovery of the turbulent boundary layer following reattachment as well as the hybrid models.

Acknowledgment

IBM SP3 computer resources were provided by a grant from the North Carolina Supercomputing Center.

References

[1]Speziale, C. G., "Turbulence Modeling for Time-Dependent RANS and VLES: A Review," *AIAA Journal*, Vol. 36, No. 2, 1998, pp. 173–184.

[2]Spalart, P. R., Jou, W.-H., Strelets, M., and Allmaras, S., "Comments on the Feasibility of LES for Wings and on a Hybrid RANS/LES Approach," *Advances in DNS/LES*, edited by C. Liu and Z. Liu, Greyden Press, Columbus, OH, 1997, pp. 137–147.

[3]Spalart, P. R., and Allmaras, S. R., "A One-Equation Turbulence Model for Aerodynamic Flows," *La Recherche Aérospatiale*, Vol. 1, No. 1, 1994, pp. 5–21.

[4]Baurle, R. A., Tam, C. J., Edwards, J. R., and Hassan, H. A., "Hybrid Simulation Approach for Cavity Flows: Blending, Algorithm, and Boundary Treatment Issues," *AIAA Journal*, Vol. 41, No. 8, 2003, pp. 1463–1480.

[5]Xiao, X., Edwards, J. R., Hassan, H. A., and Baurle, R. A., "Inflow Boundary Conditions for Hybrid Large Eddy/Reynolds Averaged Navier–Stokes Simulations," *AIAA Journal*, Vol. 41, No. 8, 2003, pp. 1481–1489.

[6]Fan, C.-C., Xiao, X., Edwards, J. R., Hassan, H. A., and Baurle, R. A., "Hybrid Large-Eddy/Reynolds-Averaged Navier–Stokes Simulations of Shock-Separated Flows," *Journal of Spacecraft and Rockets* (to be published).

[7]Mentor, F. R., "Two Equation Eddy Viscosity Turbulence Models for Engineering Applications," *AIAA Journal*, Vol. 32, No. 8, 1994, pp. 1598–1605.

[8]Settles, G. S., and Dodson, L. J., "Hypersonic Shock/Boundary-Layer Interaction Database," NASA Contractor Rept. 177577, April 1991.

[9]Settles, G. S., Williams, D. R., Baca, B. K., and Bogdonoff, S. M., "Reattachment of a Compressible Turbulent Free Shear Layer," *AIAA Journal*, Vol. 20, No. 1, 1982, pp. 60–67.

[10]Herrin, J., and Dutton, J., "Supersonic Base Flow Experiments in the Near Wake of a Cylindrical Afterbody," *AIAA Journal*, Vol. 32, No. 1, 1994, pp. 77–83.

[11]Zheltovodov, A. A., Zaulichnii, E. G., Trofimov, V. M., and Yakolev, V. N., "Heat Transfer and Turbulence Study in Compressible Separated Flows," Inst. of Theoretical and Applied Mechanics, Preprint 22-87, Russian Academy of Sciences, Novosibirsk, Russia, 1987.

[12]Robinson, D. F., and Hassan, H. A., "Further Development of the k–ζ (Enstrophy) Turbulence Closure Model," *AIAA Journal*, Vol. 36, No. 10, 1998, pp. 1825–1833.

[13]Urbin, G., and Knight, D., "Large-Eddy Simulation of a Supersonic Boundary Layer Using an Unstructured Grid," *AIAA Journal*, Vol. 39, No. 7, 2001, pp. 1288–1295.

[14]Edwards, J. R., "A Low Diffusion Flux Splitting Scheme for Navier–Stokes Calculations," *Computers and Fluids*, Vol. 26, No. 6, 1997, pp. 635–659.

[15]Dolling, D., and Murphy, M., "Unsteadiness of the Separation Shock Wave Structure in a Supersonic Compression Ramp Flowfield," *AIAA Journal*, Vol. 23, No. 12, 1983, pp. 1628–1634.

S. Aggarwal
Associate Editor